SCIENCE CHINA
Information Sciences

• RESEARCH PAPER •

June 2024, Vol. 67, Iss. 6, 162401:1–162401:9
https://doi.org/10.1007/s11432-023-3835-4

Lead-free perovskites-based photonic synaptic devices with zero electric energy consumption

Dandan HAO[1†], Di YANG[2†], Haixia LIANG[3], Jia HUANG[3,4*] & Fukai SHAN[1*]

[1]*College of Electronics and Information, Qingdao University, Qingdao* 266071*, China;*
[2]*Key Laboratory of Biofuels, Qingdao Institute of Bioenergy and Bioprocess Technology, Chinese Academy of Sciences, Qingdao* 266101*, China;*
[3]*School of Materials Science and Engineering, Tongji University, Shanghai* 201804*, China;*
[4]*National Key Laboratory of Autonomous Intelligent Unmanned Systems, Tongji University, Shanghai* 201804*, China*

Received 25 May 2023/Revised 20 June 2023/Accepted 27 July 2023/Published online 20 February 2024

Abstract The von Neumann bottleneck is a critical limitation in synaptic devices. Therefore, artificial synaptic devices resembling biological neuromorphic synapses have been developed to overcome the von Neumann bottleneck. However, synaptic devices require voltages, which results in considerable energy consumption. Here, photonic synaptic devices with the vertical structure of indium tin oxide (ITO)/SnO_2/Al_2O_3/$CsBi_3I_{10}$/Au are fabricated, which can work in the self-powered mode owing to the photovoltaic effect endowed by a vertical multilayer structure. Several fundamental synaptic functions, such as excitatory postsynaptic current, paired-pulse facilitation, short-term plasticity (STP), long-term plasticity (LTP), pulse-frequency-dependent plasticity, transition of STP to LTP, and the learning experience are emulated. Moreover, Morse-coded external light information is decoded by self-powered photonic synaptic devices. The results indicate that self-powered photonic synaptic devices based on lead-free perovskites exhibit great potential for efficient neuromorphic computing and optical wireless communication.

Keywords photonic synaptic devices, lead-free perovskites, zero energy consumption, synaptic plasticity, Morse code

1 Introduction

Artificial intelligence neural networks of modern computer systems are restricted by power consumption when dealing with complex tasks resulting from the physical separation of the memory and processor in the conventional von Neumann architecture [1,2]. Human brains with synaptic connections between 10^{11} neurons and 10^{15} synapses are highly efficient biological computing systems, in which synapses can cope with sophisticated tasks with an extremely low power consumption of 10 fJ [3–5]. Inspired by the efficient computation of human brains, artificial synaptic devices were proposed to emulate biological synaptic behaviors at the hardware level.

Various artificial synaptic devices, such as memristors [6, 7], synaptic transistors [8], atomic-switch memory [9], have been developed to mimic fundamental synaptic behaviors by using a series of electrical pulses or light pulses. However, external voltages are used to read the generated output signals of these devices. These voltages increase power consumption. Therefore, fabricating synaptic devices without electric energy consumption becomes critical for achieving neuromorphic computing with an ultralow energy consumption. The photovoltaic effect could cause the device to operate under light illumination without an external voltage. For example, the self-powered photodetector based on the photovoltaic effect can respond to the light signal at 0 V [10]. Therefore, photonic synaptic devices with zero electric energy consumption can be realized by inducing the photovoltaic effect in the synaptic device.

Metal halide perovskites (MHPs), as one of the high-efficient photovoltaic materials, have been widely utilized in solar cells, photodetectors, and light-emitting diodes because of their high optical absorption

* Corresponding author (email: huangjia@tongji.edu.cn, fkshan@qdu.edu.cn)
† Hao D D and Yang D have the same contribution to this work.

and photoelectric conversion performances [11–13]. Except for the conventional applications, MHPs have been applied in photonic synaptic devices for simulating biological synaptic functionalities [14, 15]. Previously reported MHPs-based photonic synaptic devices are mainly based on lead-based perovskites, which are hazardous to the environment and human health. Therefore, fabricating photonic synaptic devices with low energy consumption using lead-free perovskites is a critical topic of research.

In this work, self-powered photonic synaptic devices with a vertical structure of indium tin oxide (ITO)/SnO_2/Al_2O_3/$CsBi_3I_{10}$/Au ($CsBi_3I_{10}$-SPPSs) were fabricated. SnO_2 and $CsBi_3I_{10}$ were the electron transporting and light active layers, respectively. An ultrathin Al_2O_3 layer was introduced to induce interfacial trapping sites. Because of the photovoltaic effect, $CsBi_3I_{10}$-SPPSs can generate light current under the stimulation of light pulses at zero bias, which results in zero electrical energy consumption. In the self-powered mode, the $CsBi_3I_{10}$-SPPS can mimic major synaptic behaviors, including excitatory postsynaptic current (EPSC), paired-pulse facilitation (PPF), short-term plasticity (STP), and long-term plasticity (LTP). The transfer of STP to LTP and "learning experience" were emulated by regulating pulse signals. Crucially, the $CsBi_3I_{10}$-SPPS can decode Morse-coded external light information, which indicates considerable potential in wireless light communication. Therefore, lead-free perovskite-based photonic synaptic devices with zero power consumption can promote the development of high-efficiency artificial neural systems.

2 Materials and method

2.1 Materials

ITO substrates were purchased from Advanced Election Technology Co., Ltd. SnO_2 colloid precursor was offered by Alfa Aesar. Bismuth (III) Iodide (BiI_3, 99%), Cesium Iodide (CsI, 99.99%), *N*, *N*-dimethylformamide (DMF, 99.9%), acetone (99.5%), ethanol (99.5%), and dimethyl sulfoxide (DMSO, 99.7%) were purchased from Adamas. Trimethylaluminum (TMA) was obtained from Sigma-Aldrich.

2.2 $CsBi_3I_{10}$-SPPSs fabrication

First, ITO substrates were cleaned with acetone, ethanol, and deionized water sequentially in an ultrasonic cleaning machine. Next, ITO substrates were dried by using the N_2 flow and subsequently subjected to plasma treatment for 5 min to improve hydrophilicity. The SnO_2 colloid precursor of 0.3 mL was diluted with distilled water of 0.9 mL. The diluted SnO_2 colloid precursor was deposited onto ITO substrates at 3000 r/min for 30 s before heating for 30 min at 150°C. The precursor solution of $CsBi_3I_{10}$ was formed by dissolving 885 mg BiI_3 and 130 mg CsI in the 1 mL mixed solvent of DMF (0.8 mL) and DMSO (0.2 mL) under stirring at 70°C for 3 h. Ultrathin Al_2O_3 layers were deposited through atomic layer deposition (ALD) at 200°C using TMA and H_2O precursors. Each ALD deposition cycle consisted of one pulse of TMA (pulse time: 20 ms), 15 s of the N_2 purge, one pulse of H_2O (pulse time: 20 ms), and 20 s of the N_2 purge. The thickness of the Al_2O_3 layer with one ALD cycle was 0.09 nm. Next, the $CsBi_3I_{10}$ precursor solution was deposited on SnO_2-coated substrates with and without the Al_2O_3 layer by using the spin-coated method (3000 r/min, 60 s). These samples were subsequently annealed at 125°C for 30 min on the hot plate. Finally, 50-nm Au electrodes were evaporated on $CsBi_3I_{10}$ films to complete $CsBi_3I_{10}$-SPPS fabrication.

2.3 Characterizations and measurements

A scanning electron microscope (SEM, SU8010, Hitachi, Japan) was used to observe the morphologies of samples. The X-ray diffractometer (XRD, DX-2700, Dandong Haoyunan Instrument Co., Ltd., China) was used to investigate $CsBi_3I_{10}$ crystallinity. The absorption spectrum of the sample was measured using the ultraviolet-visible-near-infrared spectrophotometer (U-4100, Hitachi, Japan). X-ray photoelectron spectroscopy (XPS, ESCALAB 250Xi, Thermo Fisher Scientific, America) was performed to analyze sample composition. The Keithley 4200-SCS semiconductor parameter analyzer was used to record the photo-response properties of $CsBi_3I_{10}$-SPPSs.

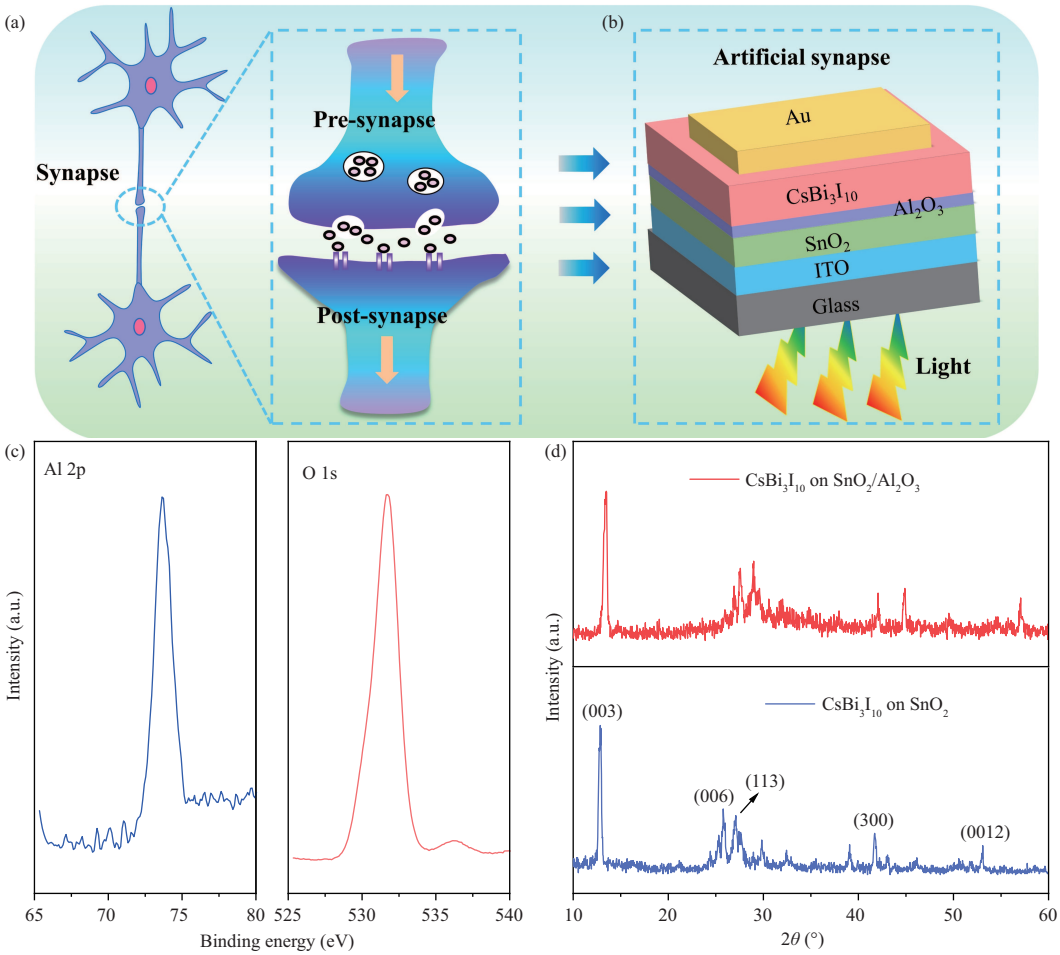

Figure 1 (Color online) Schematic of (a) a biological synapse and (b) the self-powered photonic synaptic device. (c) XPS spectrum of the Al_2O_3 layer. (d) XRD pattern of the $CsBi_3I_{10}$ film deposited on SnO_2 layer with 5 cycles of ALD-Al_2O_3.

3 Discussion and conclusion

Figure 1(a) displays a schematic of a typical biological synaptic structure. The junction between the dendrites of two neurons is depicted in the figure. Under external stimulation, discharged excitatory neurotransmitters by presynaptic neurons go across the synaptic cleft and interact with receptors on postsynaptic neurons to generate EPSC [16,17]. To mimic biological synaptic behaviors, the SPPD with a vertical architecture of ITO/SnO_2/Al_2O_3/$CsBi_3I_{10}$/Au was constructed (Figure 1(b)). Figure S1 displays the device fabrication process in which both the light absorber ($CsBi_3I_{10}$) and electron transporting layer (SnO_2) were prepared using solution methods. ALD was utilized to deposite an ultrathin Al_2O_3 layer, which was sandwiched between SnO_2 and $CsBi_3I_{10}$ layers to induce the generation of more defects in the device. ITO and Au layers were used as the cathode and anode, respectively. XPS was performed to verify the existence of the Al_2O_3 layer by scanning the cross-section of the $CsBi_3I_{10}$-SPPS. Peaks at 531.6 and 73.7 eV were attributed to O 1s and Al 2p orbitals, respectively, which indicated successful deposition of Al_2O_3 (Figure 1(c)). The XRD pattern of $CsBi_3I_{10}$ in Figure 1(d) reveals that the dominant diffraction peaks of $CsBi_3I_{10}$ deposited on the SnO_2 layer are located at 12.89°, 25.73°, and 41.77°, corresponding to the (003), (006), and (300) planes of BiI_3, respectively [18, 19]. The diffraction peaks of $CsBi_3I_{10}$ deposited on the SnO_2 layer with 5 cycles of ALD-Al_2O_3 shifted to the high angles; this phenomenon may result from the doping effect of Al atoms with small atomic radius [20]. XPS characterization was utilized to investigate the chemical nature and binding energies of $CsBi_3I_{10}$ (Figure S2). Peaks at 724.46, 738.45, 156.39, 163.69, 618.82, and 630.35 eV were attributed to Cs $3d_{5/2}$, Cs $3d_{3/2}$, Bi $4f_{7/2}$, Bi $4f_{5/2}$, I $3d_{5/2}$, and I $3d_{5/2}$ orbitals, respectively (Figure S2(b)).

In the biological nervous system, the EPSC behavior is used for information transmission, processing,

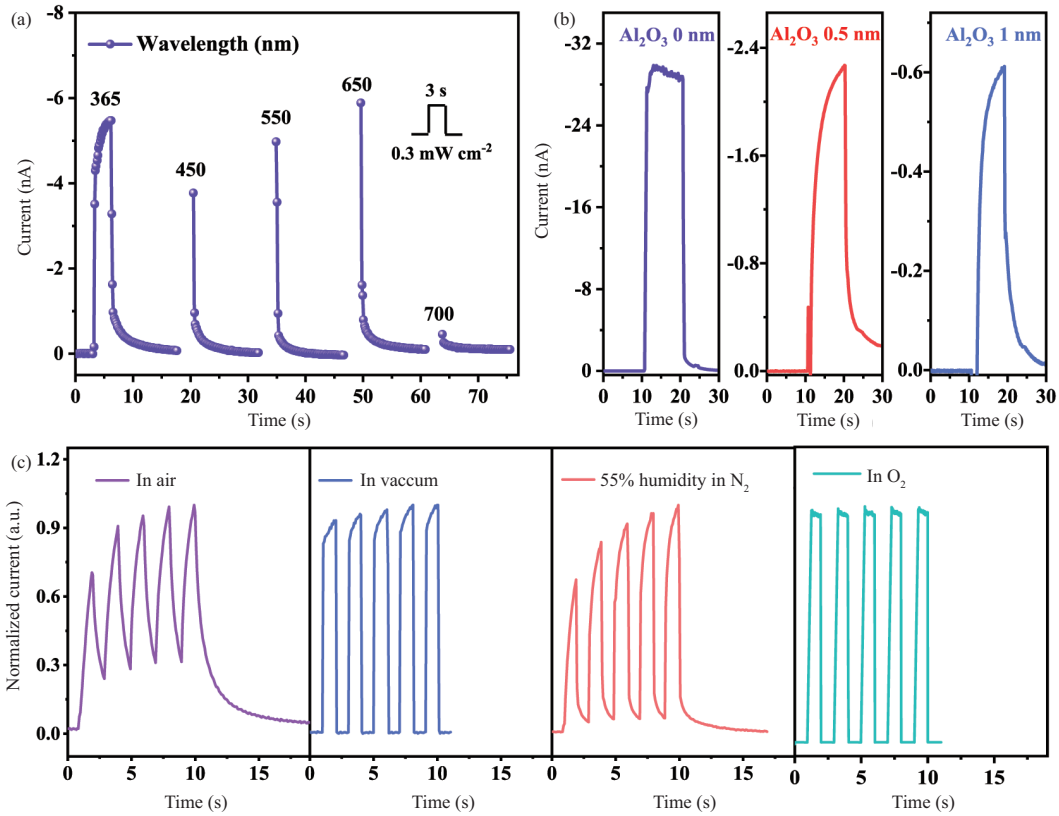

Figure 2 (Color online) (a) Temporal light responses of the $CsBi_3I_{10}$-SPPS under light illumination (3 s, 0.3 mW·cm^{-2}) with various wavelengths. (b) Photo-responses of devices with 0, 5, and 10 cycles of ALD-Al_2O_3, which were triggered by the same light pulse (10 s, 1 mW·cm^{-2}). (c) EPSC characteristics of the $CsBi_3I_{10}$-SPPS under various atmospheres (air, vacuum, 55% humidity in N_2, and O_2, respectively).

and storage. EPSC can be excited by light stimulus and subsequently returned to the initial value after turning off the optical illumination in artificial photonic synapses. Therefore, first, we investigated the EPSC behavior of the $CsBi_3I_{10}$-SPPS under light pulses of distinct wavelengths. Figure 2(a) reveals that the light current increased rapidly to a peak value under the light excitation of the fixed wavelength and subsequently decreased gradually to its initial state after removing the light stimulus for a period. Such light response of the $CsBi_3I_{10}$-SPPS is in accordance with the EPSC behavior in biological synapses. Moreover, the $CsBi_3I_{10}$-SPPS has a higher photoresponsivity at 650 nm, which indicates an excellent uniformity with the absorption spectrum of the $CsBi_3I_{10}$ film (Figure S3). Thus, the 650-nm light was utilized as the input signal to trigger the $CsBi_3I_{10}$-SPPS.

To investigate the effect of the Al_2O_3 layer on synaptic behaviors, devices with different cycles (0, 5, and 10) of ALD-Al_2O_3 were prepared. The EPSC behaviors of the devices were evoked by a 10 s light pulse (650 nm, 0.1 mW·cm^{-2}). As displayed in Figure 2(b), the device without an Al_2O_3 layer exhibited high light current and fast photo-switching property because of the effective separation of photo-induced electron-holes pairs at the interfaces of $SnO_2/CsBi_3I_{10}$ (Figure S4(a)). With the increase in the thickness of the Al_2O_3 layer, the photocurrent of the device decreased, which could be attributed to the obstruction effect of Al_2O_3 to electrons owing to the increased insulating performance of Al_2O_3 (Figure S4(b)) [21]. For the device with 5 and 10 cycles of ALD-Al_2O_3, the current decay was obtained after the removal of the light signal. The device with 5 cycles ALD-Al_2O_3 exhibited a longer memory time compared with that without ALD-Al_2O_3. Therefore, the device with 5 cycles ALD-Al_2O_3 was selected as the artificial photonic synaptic device, considering its high EPSC value under the stimulus and long retention time after removing the light. To investigate the EPSC behavior of the device, the surface morphologies of $CsBi_3I_{10}$ with various cycles of ALD-Al_2O_3 were characterized (Figure S5). The $CsBi_3I_{10}$ film deposited on 5 cycles of ALD-Al_2O_3 layer possessed a few holes, whereas $CsBi_3I_{10}$ films on 0 and 10 cycles of ALD-Al_2O_3 were dense. These holes in perovskite films could absorb water and oxygen molecules, which could act as charge-trapping sites for capturing charge carriers to generate EPSC behaviors. Therefore,

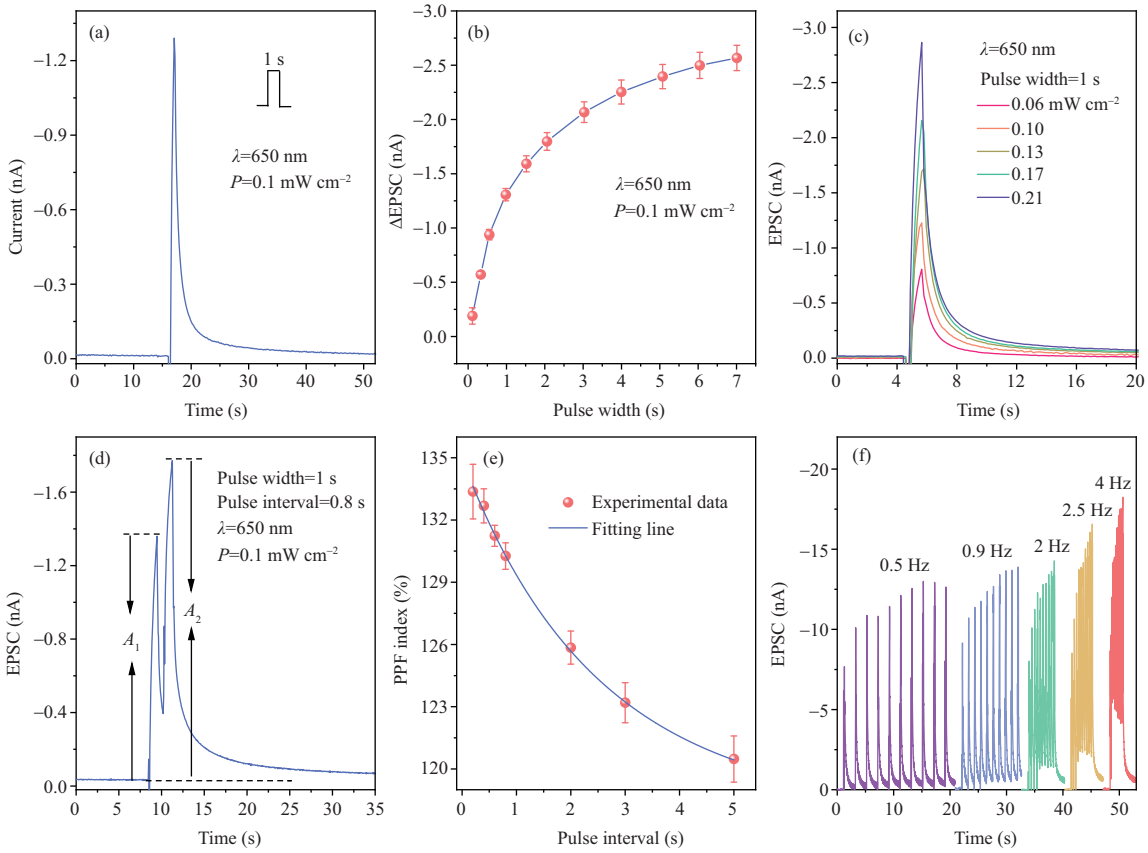

Figure 3 (Color online) (a) Typical EPSC behavior of the $CsBi_3I_{10}$-SPPS under light stimulus (650 nm, 0.1 mW·cm^{-2}). (b) Dependence of ΔEPSC on pulse widths. (c) EPSC response of the $CsBi_3I_{10}$-SPPS under various light intensities. (d) EPSC triggered by a pair of light pulses with an interval of 0.8 s. (e) Relationship between the PPF index and pulse interval. Pulse width and pulse intensity were fixed at 1 s and 0.1 mW·cm^{-2}, respectively. (f) EPSC at pulse frequencies from 0.5 to 4 Hz. The pulse intensity is 0.45 mW·cm^{-2}.

control experiments were performed to investigate the contributing factors of synaptic performance. In these experiments, 5 successive light pulses were used for the $CsBi_3I_{10}$-SPPS, and the EPSC behaviors under various environments (air, vacuum, N_2 atmosphere with 55% humidity, and O_2 atmosphere) were measured. As shown in Figure 2(c), $CsBi_3I_{10}$-SPPS exhibited fast photo-switching properties in both vacuum and O_2 atmospheres, which excludes the possibility of oxygen molecules causing the synaptic behavior. The peak current increased gradually with the light pulse number when the device was exposed to N_2 atmosphere with 55% humidity. This phenomenon indicated the effect of absorbed water molecules on synaptic functions. The adsorbed water could behave as the electron donor [22–24]. Therefore, light-generated holes would be captured by the adsorbed water, causing a longer lifetime than the transit time. In addition, defects at the interfaces among SnO_2, Al_2O_3, and $CsBi_3I_{10}$ or grain boundaries of materials could function as trapping sites to induce the interface charge capture and release before and after light stimulation (Figure S6) [25, 26].

$CsBi_3I_{10}$-SPPSs mimicked representative synaptic functions in ambient air in the self-powered mode. A light stimulus of 650 nm with an intensity of 0.1 mW·cm^{-2} and pulse width of 1 s was utilized to excite the $CsBi_3I_{10}$-SPPS for generating EPSC. As shown in Figure 3(a), the EPSC reached a peak value of −1.3 nA at the end of the light stimulus and gradually decayed to its initial state within more than 30 s. Except for working at 0 V, the typical EPSC behaviors were observed at various voltages of −0.2, −0.3, and −0.4 V (Figure S7). The pulse-width-dependent plasticity of the $CsBi_3I_{10}$-SPPS was investigated, as displayed in Figure 3(b). ΔEPSC increased from −0.19 to −2.57 nA as the pulse width enhanced from 0.1 to 7 s. Enhanced ΔEPSC could be ascribed to the increased photo-generated charge carriers under long periods of light. The saturation phenomenon of ΔEPSC was presented when the pulse width increased to a few seconds. This phenomenon could be attributed to the equilibrium between the generation and recombination of photo-induced charge carriers. This phenomenon is essentially accordant

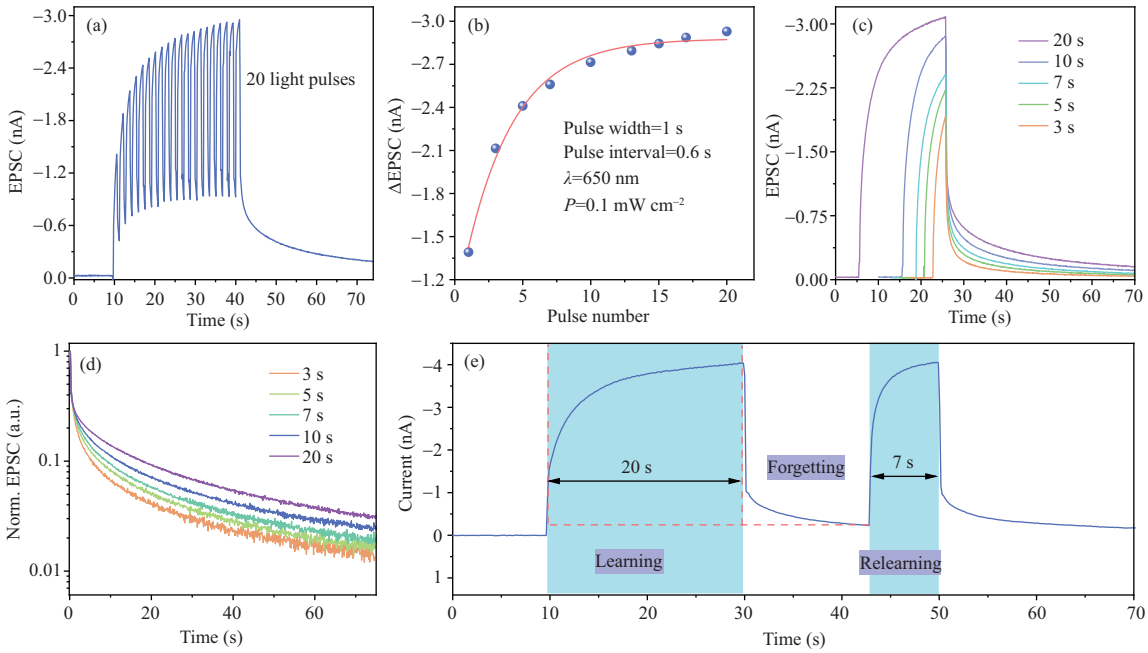

Figure 4 (Color online) (a) EPSC evoked by 20 light pulses (650 nm, 0.1 mW·cm^{-2}) with the pulse width and pulse interval of 1 and 0.6 s. (b) ΔEPSC dependence on the pulse number. (c) EPSC evoked by the light pulse (650 nm, 0.1 mW·cm^{-2}) with various pulse widths (3, 5, 7, 10, and 20 s). (d) Decay processes of EPSCs after removing light pulses with various pulse widths. (e) Learning experience behavior stimulated by the light pulse.

with the relationship between ΔEPSC and the pulse width in biological synapses [27,28]. Moreover, the EPSC of the $CsBi_3I_{10}$-SPPS could be affected by light intensity. Figure 3(c) displays EPSC values and retention time increase gradually with light intensity. The ΔEPSC value increased from −0.75 to −2.8 nA as the light intensity increased from 0.06 to 0.21 mW·cm^{-2} (Figure S8). Crucially, the $CsBi_3I_{10}$-SPPS can realize an obvious EPSC response under a very weak light stimulation of 0.001 mW·cm^{-2} and a short pulse width of 0.5 s (Figure S9). PPF, as a typical STP, has an important meaning in decoding temporal information [29]. Therefore, two successive light signals (0.1 mW·cm^{-2}, 1 s) with a pulse interval of 0.8 s were applied to the $CsBi_3I_{10}$-SPSS to emulate the PPF behavior. Figure 3(d) displays that the EPSC provoked by the second light pulse is higher than that induced by the first pulse. Figure 3(e) displays the dependence of the PPF index ($A_2/A_1 \times 100\%$, A_2 and A_1 are the maximum ΔEPSC values triggered by the second and first pulse, respectively) on the pulse interval. A maximum PPF index of 133% was obtained at the pulse interval of 0.2 s, and the PPF index decreased with the increase of the pulse interval. The results could be attributed to the following reason. A part of the photo-induced holes generated by the first pulse was still kept in trapping sites in the $CsBi_3I_{10}$-SPPS, which caused A_2 to be larger than A_1. However, the trapped holes released gradually as the pulse interval increased, which resulted in fewer residual trapped holes in defect sites after a long pulse interval. Therefore, a high PPF index can be obtained under a short pulse interval. Furthermore, ten light pulses (0.1 mW·cm^{-2}) with various frequencies from 0.5 to 4 Hz were employed to the $CsBi_3I_{10}$-SPPS for investigating the pulse-frequency-dependent plasticity of the $CsBi_3I_{10}$-SPPS. Figure 3(f) presents the EPSC response in each pulse train under various frequencies, in which the enhancement of EPSC can be obtained as a function of frequency. The EPSC gain (A_{10}/A_1) was used to investigate the potentiation of EPSC triggered by a series of light pulses with various frequencies. Here, A_{10} is the maximum value of ΔEPSC induced by the tenth light pulse. With the increase of the pulse frequency from 0.5 to 4 Hz, the EPSC gain elevated from 1.6 to 2.1 (Figure S10), which indicates the $CsBi_3I_{10}$-SPPS can transfer information in the form of the dynamic high-pass filter [30].

Figure 4(a) shows the EPSC triggered by 20 successive light pulses with pulse width and interval of 1 and 0.6 s, respectively. With the enhancement of the light pulse number, the EPSC value gradually increased and the corresponding relationship between ΔEPSC and light pulse number is presented in Figure 4(b). A nonlinear increase was observed in ΔEPSC with the light pulse number, which was similar to the learning process in human brains. This learning behavior can be fitted by the following

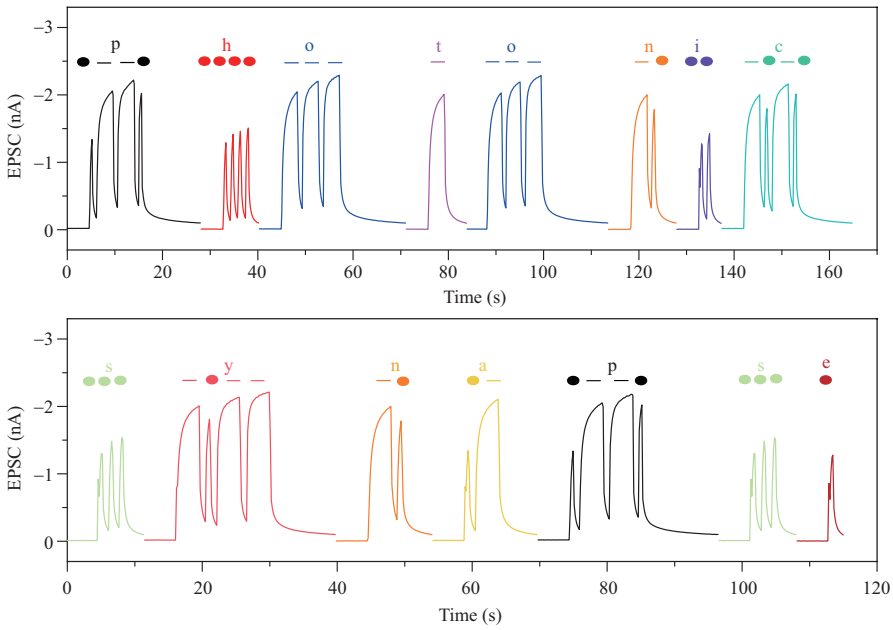

Figure 5 (Color online) Light-evoked EPSCs expressing the Morse code of "photonic synapse" by orderly illuminating the $CsBi_3I_{10}$-SPPS.

equation [31]:

$$\gamma = \gamma_0 + A \times \exp\left(\frac{N}{\tau_1}\right),$$

where N is the light pulse number, A is the initial facilitation value during learning process, γ_0 is the resting facilitation value, and τ_1 is the learning time in the $CsBi_3I_{10}$-SPPS. The learning curve in Figure 4(b) displays that the $CsBi_3I_{10}$-SPPS exhibits a fast learning at the beginning of the stimulation and then tends to a slow even saturated learning with the enhancement of rehearsals. Figure S11 displays the decay processes of the normalized EPSC after light illumination with pulses of 3, 7, 10, and 20. An elevated memory level was observed with the increase of the light pulse number. This result indicates that the $CsBi_3I_{10}$-SPPS can emulate the transition from STP to LTP of human brains during the repetitive learning process. Moreover, this transition process was also achieved by modulating pulse widths. As displayed in Figures 4(c) and (d), the enhanced EPSC value and long decay time were observed under a long pulse width. Furthermore, the learning experience behavior in a biological synapse was simulated by using the $CsBi_3I_{10}$-SPPS. The learning experience behavior describes that a person gradually acquires knowledge through learning, and the remembered knowledge is forgotten slowly with the lapse of time. However, less time is required to remember the same knowledge when the person learns the same thing again [32,33]. As displayed in Figure 4(e), a light stimulus of 0.1 mW·cm^{-2} was used to the $CsBi_3I_{10}$-SPPS in the self-powered mode. The EPSC of the device increased from −0.25 to −4.05 nA in 20 s during the first light stimulus process. However, when the EPSC decayed to −0.25 nA after the removal of the first stimulus, only 7 s were required for the second light pulse to induce the EPSC to increase from −0.25 to −4.05 nA. This process suggests that the $CsBi_3I_{10}$-SPPS can emulate the "learning-forgetting-relearning" behavior of human beings.

Morse code, as one of the forms of digital communication, shows characters of dots and dashes by using a canonical sequence of two signal widths. Moreover, the human brain can sense Morse codes in various forms such as light, sound, and pressure [34]. Coded light information can be decoded by differentiating induced width-dependent EPSC by exciting the $CsBi_3I_{10}$-SPPS orderly in a Morse code pattern. By illuminating the $CsBi_3I_{10}$-SPPS using light pulses with various pulse widths (1 and 3 s, respectively), dot and dash patterns were encoded. The light intensity and pulse interval were set to 0.1 mW·cm^{-2} and 1 s, respectively. As displayed in Figure 5, the coded light information of "photonic" and "synapse" was decoded by orderly exciting the $CsBi_3I_{10}$-SPPS using various combining forms of dots and dashes, such as "h" is four dots (0.1 mW·cm^{-2}, 1 s), "o" is three dashes (0.1 mW·cm^{-2}, 3 s), and "n" is the combination of one dash and one dot. Various EPSC amplitudes were obtained in Figure 5 under the stimulation of different combining forms of dots and dashes, which expressed "photonic" and "synapse". The results

indicated that $CsBi_3I_{10}$-SPPSs exhibited considerable potential for optical wireless communication in the future.

In summary, SPPSs with a vertical structure of ITO/SnO_2/Al_2O_3/$CsBi_3I_{10}$/Au have been fabricated. $CsBi_3I_{10}$-SPPSs can be operated in the self-powered mode owing to the photovoltaic effect endowed by the vertical multilayer structure. An ultrathin Al_2O_3 layer was responsible for the generation of trap sites in perovskites and surfaces of various layers. The trapping and release of photo-generated charge carriers rendered the simulation of synaptic plasticity. Compared with the previously reported perovskite-based photonic synapses, $CsBi_3I_{10}$-SPPSs can ensure both environmental friendliness and zero power consumption (Table S1). $CsBi_3I_{10}$-SPPSs can emulate fundamental synaptic functions such as EPSC, PPF, STP, LTP, STP to LTP transition, and "learning experience" in the self-powered mode and achieve zero electric energy consumption. Furthermore, $CsBi_3I_{10}$-SPPSs can decode Morse-coded external light information. The results indicated that SPPSs based on lead-free perovskites have great potential for neuromorphic computing and optical wireless communication.

Acknowledgements This work was supported by National Key Research and Development Program of China (Grant Nos. 2021YFA1101303, 2019YFE0121800), Science & Technology Foundation of Shanghai (Grant No. 20JC1415600), National Natural Science Foundation of China (Grant Nos. 62074111, 62088101), Innovation Program of Shanghai Municipal Education Commission (Grant No. 2021-01-07-00-07-E00096), Shanghai Municipal Science and Technology Major Project (Grant No. 2021SHZDZX0100), and Natural Science Foundation of Shandong Province (Grant Nos. ZR2022QB009, ZR2022MF246).

Supporting information Figures S1–S11, Table S1. The supporting information is available online at info.scichina.com and link.springer.com. The supporting materials are published as submitted, without typesetting or editing. The responsibility for scientific accuracy and content remains entirely with the authors.

References

1 Yu R, Li E, Wu X, et al. Electret-based organic synaptic transistor for neuromorphic computing. ACS Appl Mater Interface, 2020, 12: 15446–15455
2 Gong Y, Wang Y, Li R, et al. Tailoring synaptic plasticity in a perovskite QD-based asymmetric memristor. J Mater Chem C, 2020, 8: 2985–2992
3 Wang T Y, Meng J L, He Z, et al. Ultralow power wearable heterosynapse with photoelectric synergistic modulation. Adv Sci, 2020, 7: 1903480
4 Liu Y, Zhong J, Li E, et al. Self-powered artificial synapses actuated by triboelectric nanogenerator. Nano Energy, 2019, 60: 377–384
5 Wang W, Gao S, Wang Y, et al. Advances in emerging photonic memristive and memristive-like devices. Adv Sci, 2022, 9: 2105577
6 Zhang Y, Wang Z, Zhu J, et al. Brain-inspired computing with memristors: challenges in devices, circuits, and systems. Appl Phys Rev, 2020, 7: 011308
7 Mao H, Zhu Y, Zhu Y, et al. Amorphous indium-gallium-zinc-oxide memristor arrays for parallel true random number generators. Appl Phys Lett, 2023, 122: 053503
8 Li E, Lin W, Yan Y, et al. Synaptic transistor capable of accelerated learning induced by temperature-facilitated modulation of synaptic plasticity. ACS Appl Mater Interface, 2019, 11: 46008–46016
9 Wang Z, Joshi S, Savel'ev S E, et al. Memristors with diffusive dynamics as synaptic emulators for neuromorphic computing. Nat Mater, 2017, 16: 101–108
10 Cao F, Tian W, Deng K, et al. Self-powered UV-Vis-NIR photodetector based on conjugated-polymer/$CsPbBr_3$ nanowire array. Adv Funct Mater, 2019, 29: 1906756
11 Hu L, Zhao Q, Huang S, et al. Flexible and efficient perovskite quantum dot solar cells via hybrid interfacial architecture. Nat Commun, 2021, 12: 466
12 Dong Y, Wang Y K, Yuan F, et al. Bipolar-shell resurfacing for blue LEDs based on strongly confined perovskite quantum dots. Nat Nanotechnol, 2020, 15: 668–674
13 Zhang Z X, Li C, Lu Y, et al. Sensitive deep ultraviolet photodetector and image sensor composed of inorganic lead-free $Cs_3Cu_2I_5$ perovskite with wide bandgap. J Phys Chem Lett, 2019, 10: 5343–5350
14 Wang Y, Lv Z, Chen J, et al. Photonic synapses based on inorganic perovskite quantum dots for neuromorphic computing. Adv Mater, 2018, 30: 1802883
15 Hao D D, Yang Z Y, Huang J, et al. Recent developments of optoelectronic synaptic devices based on metal halide perovskites. Adv Funct Mater, 2023, 33: 2211467
16 Kumar M, Abbas S, Lee J H, et al. Controllable digital resistive switching for artificial synapses and Pavlovian learning algorithm. Nanoscale, 2019, 11: 15596–15604
17 Li Y, Wang Y, Yin L, et al. Silicon-based inorganic-organic hybrid optoelectronic synaptic devices simulating cross-modal learning. Sci China Inf Sci, 2021, 64: 162401
18 Hao D, Liu D, Shen Y, et al. Air-stable self-powered photodetectors based on lead-free $CsBi_3I_10/SnO_2$ heterojunction for weak light detection. Adv Funct Mater, 2021, 31: 2100773
19 Liu Z, Dai S, Wang Y, et al. Photoresponsive transistors based on lead-free perovskite and carbon nanotubes. Adv Funct Mater, 2020, 30: 1906335
20 Ji F, Huang Y, Wang F, et al. Near-infrared light-responsive Cu-doped Cs_2 $AgBiBr_6$. Adv Funct Mater, 2020, 30: 2005521
21 Yuan Y, Zhang L, Yan G, et al. Significantly enhanced detectivity of CIGS broadband high-speed photodetectors by grain size control and ALD-Al_2O_3 interfacial-layer modification. ACS Appl Mater Interface, 2019, 11: 20157–20166
22 Meng Y, Li F Z, Lan C Y, et al. Artificial visual systems enabled by quasi-two-dimensional electron gases in oxide superlattice nanowires. Sci Adv, 2020, 6: 6389
23 Park J S, Jeong J K, Chung H J, et al. Electronic transport properties of amorphous indium-gallium-zinc oxide semiconductor upon exposure to water. Appl Phys Lett, 2008, 92: 072104

24 Jeong J K, Yang H W, Jeong J H, et al. Origin of threshold voltage instability in indium-gallium-zinc oxide thin film transistors. Appl Phys Lett, 2008, 93: 123508
25 Guo Z, Liu J, Han X, et al. High-performance artificial synapse based on CVD-grown WSe_2 flakes with intrinsic defects. ACS Appl Mater Interface, 2023, 15: 19152–19162
26 Hao D, Zhang J, Dai S, et al. Perovskite/organic semiconductor-based photonic synaptic transistor for artificial visual system. ACS Appl Mater Interface, 2020, 12: 39487–39495
27 Yang Y, Lisberger S G. Purkinje-cell plasticity and cerebellar motor learning are graded by complex-spike duration. Nature, 2014, 510: 529–532
28 Huang W, Hang P, Wang Y, et al. Zero-power optoelectronic synaptic devices. Nano Energy, 2020, 73: 104790
29 Dai S, Wu X, Liu D, et al. Light-stimulated synaptic devices utilizing interfacial effect of organic field-effect transistors. ACS Appl Mater Interface, 2018, 10: 21472–21480
30 Sun Y, Qian L, Xie D, et al. Photoelectric synaptic plasticity realized by 2D perovskite. Adv Funct Mater, 2019, 29: 1902538
31 Ahmed T, Kuriakose S, Mayes E L H, et al. Optically stimulated artificial synapse based on layered black phosphorus. Small, 2019, 15: 1900966
32 Ma F, Zhu Y, Xu Z, et al. Optoelectronic perovskite synapses for neuromorphic computing. Adv Funct Mater, 2020, 30: 1908901
33 Wang T Y, Meng J L, He Z Y, et al. Fully transparent, flexible and waterproof synapses with pattern recognition in organic environments. Nanoscale Horiz, 2019, 4: 1293–1301
34 Yu F, Cai J C, Zhu L Q, et al. Artificial tactile perceptual neuron with nociceptive and pressure decoding abilities. ACS Appl Mater Interface, 2020, 12: 26258–26266